

Article

# Periodic Trends in Olefin Epoxidation over Group IV and V Framework Substituted Zeolite Catalysts: A Kinetic and Spectroscopic Study

Daniel T Bregante, and David W. Flaherty

*J. Am. Chem. Soc.*, **Just Accepted Manuscript** • Publication Date (Web): 28 Apr 2017

Downloaded from <http://pubs.acs.org> on April 29, 2017

## Just Accepted

“Just Accepted” manuscripts have been peer-reviewed and accepted for publication. They are posted online prior to technical editing, formatting for publication and author proofing. The American Chemical Society provides “Just Accepted” as a free service to the research community to expedite the dissemination of scientific material as soon as possible after acceptance. “Just Accepted” manuscripts appear in full in PDF format accompanied by an HTML abstract. “Just Accepted” manuscripts have been fully peer reviewed, but should not be considered the official version of record. They are accessible to all readers and citable by the Digital Object Identifier (DOI®). “Just Accepted” is an optional service offered to authors. Therefore, the “Just Accepted” Web site may not include all articles that will be published in the journal. After a manuscript is technically edited and formatted, it will be removed from the “Just Accepted” Web site and published as an ASAP article. Note that technical editing may introduce minor changes to the manuscript text and/or graphics which could affect content, and all legal disclaimers and ethical guidelines that apply to the journal pertain. ACS cannot be held responsible for errors or consequences arising from the use of information contained in these “Just Accepted” manuscripts.

# Periodic Trends in Olefin Epoxidation over Group IV and V Framework Substituted Zeolite Catalysts: A Kinetic and Spectroscopic Study

Daniel T. Bregante and David W. Flaherty\*

Department of Chemical and Biomolecular Engineering, University of Illinois at Urbana-Champaign, Urbana, IL, 61801, United States

**ABSTRACT:** Group IV and V framework substituted zeolites have been used for olefin epoxidation reactions for decades, yet the underlying properties that determine the selectivities and turnover rates of these catalysts have not yet been elucidated. Here, a combination of kinetic, thermodynamic, and *in situ* spectroscopic measurements show that when group IV (i.e., Ti, Zr, and Hf) or V (i.e., Nb and Ta) transition metals are substituted into zeolite \*BEA, the metals that form stronger Lewis acids give greater selectivities and rates for the desired epoxidation pathway and present smaller enthalpic barriers for both epoxidation and H<sub>2</sub>O<sub>2</sub> decomposition reactions. *In situ* UV-vis spectroscopy shows that these group IV and V materials activate H<sub>2</sub>O<sub>2</sub> to form pools of hydroperoxide, peroxide, and superoxide intermediates. Time-resolved UV-vis measurements and the isomeric distributions of stilbene epoxidation products demonstrate that the active species for epoxidations on group IV and V transition metals are only M-OOH/(O<sub>2</sub>)<sup>2-</sup> and M-(O<sub>2</sub>)<sup>-</sup> species, respectively. Mechanistic interpretations of kinetic data suggest that these group IV and V materials catalyze cyclohexene epoxidation and H<sub>2</sub>O<sub>2</sub> decomposition through largely identical Eley-Rideal mechanisms that involve the irreversible activation of coordinated H<sub>2</sub>O<sub>2</sub> followed by reaction with an olefin or H<sub>2</sub>O<sub>2</sub>. Epoxidation rates and selectivities vary over five- and two-orders of magnitude, respectively, among these catalysts and depend exponentially on the energy for ligand-to-metal charge transfer (LMCT) and the functional Lewis acid strength of the metal centers. Together these observations show that more electrophilic active-oxygen species (i.e., lower energy LMCT) are more reactive and selective for epoxidations of electron-rich olefins and explain why Ti-based catalysts have been identified as the most active among early transition metals for these reactions. Further, H<sub>2</sub>O<sub>2</sub> decomposition (the undesirable reaction pathway) possesses a weaker dependence on Lewis acidity than epoxidation, which suggests that the design of catalysts with increased Lewis acid strength will simultaneously increase the reactivity and selectivity of olefin epoxidation.

## 1.0 INTRODUCTION

Small-molecule oxidations are among the most important and well-studied reactions in synthetic chemistry.<sup>1</sup> Olefin epoxidation is of particular importance, as epoxides (e.g., propylene oxide, styrene oxide, etc.) are important precursors and monomers for the production of pharmaceuticals and epoxy resins.<sup>2-4</sup> Despite the importance of epoxides, current production methods typically involve the use of hazardous organic-peroxide oxidants<sup>4</sup> or caustic-waste producing Cl-containing processes (e.g., the chlorohydrin process).<sup>5</sup> Molecular oxygen (O<sub>2</sub>) is utilized for the epoxidation of ethylene (C<sub>2</sub>H<sub>4</sub>) to form ethylene oxide (EO) over promoted Ag catalysts.<sup>6-9</sup> However, selectivities for C<sub>2</sub>H<sub>4</sub> epoxidation with O<sub>2</sub> reach 90 %, while 5 – 10 % of C<sub>2</sub>H<sub>4</sub> is over oxidized to form massive amounts of CO<sub>2</sub> annually (1.5 – 3 Mton yr<sup>-1</sup>),<sup>6</sup> which contributes to global climate change.<sup>10</sup> Furthermore, supported Ag catalysts tend to oxidize allylic positions within hydrocarbons, which prevents the use of these catalysts and O<sub>2</sub> for the epoxidation of molecules larger than C<sub>2</sub>H<sub>4</sub>.<sup>6</sup>

Hydrogen peroxide (H<sub>2</sub>O<sub>2</sub>) is a green oxidant that can selectively epoxidize olefins and may replace more environmentally impactful oxidants. Currently, one of the few industrial processes that utilizes H<sub>2</sub>O<sub>2</sub> for olefin epoxidation is the hydrogen peroxide – propylene oxide process,<sup>4,11</sup> which couples

the anthraquinone auto-oxidation process with a propylene epoxidation facility that catalyzes propylene epoxidations with a microporous titanium silicate zeolite catalyst (TS-1).<sup>12,13</sup> TS-1 gives acceptable H<sub>2</sub>O<sub>2</sub> selectivities (80 – 95 %) for propylene epoxidation;<sup>14</sup> however, it is not obvious how other early-transition metal substituted zeolites may perform in epoxidations. Additionally, the differences of epoxidation rates and selectivities between Ti- and other early transition metal atoms in zeolite frameworks are not experimentally demonstrated in the open literature and neither are the reasons for such potential differences. Consequently, there are few proven guiding principles for the synthesis of improved microporous catalysts for epoxidations.

Group IV and V metals grafted onto SiO<sub>2</sub> or incorporated into tetrahedral sites within zeolite frameworks effectively activate H<sub>2</sub>O<sub>2</sub> and epoxidize olefins.<sup>4,15-23</sup> Monomeric Nb atoms in the \*BEA zeolite framework (Nb-β) irreversibly activate H<sub>2</sub>O<sub>2</sub> to form superoxide intermediates (i.e., Nb-(O<sub>2</sub>)<sup>-</sup>) that selectively epoxidize olefins.<sup>15</sup> Alternatively, Ti atoms within TS-1 activate H<sub>2</sub>O<sub>2</sub> to form Ti-OOH species, which are thought to be active for olefin epoxidation.<sup>24-26</sup> Several computational studies probed the effects of transition metal atom substitution into zeolite frameworks on the Lewis and Brønsted acid strengths and correlated these changes to pre-

dicted reactivity predominantly for biomass conversion or the isomerization of glucose.<sup>27-30</sup> Most relevant to this work, Boronat *et al.* used quantum chemical calculations to relate the LUMO energy of the transition metal atoms Ti, Zr, and Sn within the framework of zeolite \*BEA to the measured rates of octene epoxidation and attributed the relatively high reactivity of Ti- $\beta$  to a LUMO energy that is lower than those of Zr- and Sn- $\beta$ .<sup>31</sup> Experimentally, Notestein and coworkers found that the initial rates of cyclohexene epoxidation over group IV and V metals grafted onto silica correlate with the Pauling electronegativity of these metals.<sup>23</sup> In summary, the Lewis acidity of these heterogeneous atomically-isolated catalysts has been hypothesized to determine the ability of such species to activate H<sub>2</sub>O<sub>2</sub> and the manner by which the activated complex reacts with an olefin.<sup>22,31-36</sup> Interestingly, these trends disagree with a significant body of work on group VII and VIII (e.g., Mn and Fe) homogeneous complexes (e.g., porphyrin- and Schiff-base complexes), for which greater electron densities on the metal centers increase oxidation rates by facilitating the formation of M=O species via heterolytic cleavage of the O-O bond of H<sub>2</sub>O<sub>2</sub>.<sup>4,37</sup> Connections between the Lewis acid strength of metal-substituted zeolites and epoxidation rates and selectivities have been hypothesized to exist for nearly two decades.<sup>23,31,35,36</sup> However, to the best of our knowledge, no investigations have correlated barriers for epoxidation and H<sub>2</sub>O<sub>2</sub> decomposition (i.e., to infer selectivity) to *experimentally* determined descriptors of the strength of the Lewis acid sites or to the electronic structure of the reactive surface intermediates for epoxidation. Furthermore, no studies have compared the identities and relative reactivities of the active hydroperoxo and superoxo intermediates for epoxidation or the ways in which their electronic structures reflect the chemical properties of the transition metal heteroatom on these group IV and V metal substituted zeolite catalysts.

Here, we incorporate group IV (i.e., Ti, Zr, and Hf) and V (i.e., Nb, and Ta) metal atoms into the framework of zeolite \*BEA (M- $\beta$ ) and use reaction rates measured as a function of the reactant concentrations to show that these M- $\beta$  catalysts catalyze H<sub>2</sub>O<sub>2</sub> decomposition and cyclohexene (C<sub>6</sub>H<sub>10</sub>) epoxidation through an identical mechanism that varies only in the structure of the active oxidant. H<sub>2</sub>O<sub>2</sub> activates irreversibly to form dioxygen intermediates (M-(O<sub>2</sub>)), such as M-(O<sub>2</sub>)<sup>-</sup> or M-OOH/-(O<sub>2</sub>)<sup>2-</sup>, which subsequently react with C<sub>6</sub>H<sub>10</sub> through an Eley-Rideal mechanism to form cyclohexene oxide (C<sub>6</sub>H<sub>10</sub>O) or with H<sub>2</sub>O<sub>2</sub> to decompose. *In situ* UV-vis measurements and the distributions of isomeric products from Z-stilbene epoxidation demonstrate that only M-(O<sub>2</sub>)<sup>-</sup> species participate directly in epoxidation on group V Lewis acid sites, whereas only M-OOH/-(O<sub>2</sub>)<sup>2-</sup> intermediates react to form epoxides on group IV Lewis acid sites. Reaction rates and selectivities depend exponentially on the extent of electron exchange between these active intermediates and the metal centers, as shown by the energy of the ligand-to-metal charge transfer (LMCT) bands. The thermodynamic strengths of the Lewis acidic metal centers were quantified from adsorption isobars for deuterated acetonitrile and compared to activation enthalpies ( $\Delta H^\ddagger$ ) for both pathways. These comparisons show that stronger Lewis acids possess *both* lower  $\Delta H^\ddagger$  (i.e., increased reactivity) and higher selectivities for the epoxidation of C<sub>6</sub>H<sub>10</sub> by M-(O<sub>2</sub>) intermediates. Collectively, these results demonstrate that the rates for catalytic epoxidation on these M- $\beta$  materials (and likely that in other zeolite frameworks) directly reflect the strength of the Lewis acid site and elucidate the reasons for

observed selectivity trends on similar group IV and V heterogeneous catalysts.

## 2.0 EXPERIMENTAL METHODS

### 2.1 Catalyst Synthesis

Group IV and V transition metal atoms were incorporated into tetrahedral positions of the \*BEA framework by either solid-state<sup>38</sup> (Zr and Hf) or liquid-phase<sup>15,39,40</sup> (Nb, Ta, and Ti) metal-atom incorporation of dealuminated \*BEA following previously published procedures. In short, commercial \*BEA (Zeolyst, Si:Al ~ 12.5, NH<sub>4</sub><sup>+</sup> cation) was contacted with concentrated HNO<sub>3</sub> (Macron Chemicals, 69-70 wt. %, 20 cm<sup>3</sup> HNO<sub>3</sub> g<sub>zeolite</sub><sup>-1</sup>) at reflux (448 K) for 20 h with the intent to remove Al atoms from the framework to produce solvated Al(NO<sub>3</sub>)<sub>3</sub>. Afterwards, the solids were recovered by filtration and washed first with concentrated HNO<sub>3</sub> and then with deionized H<sub>2</sub>O (17.8 M $\Omega$ ). The recovered solids were then heated to 823 K at 5 K min<sup>-1</sup> under flowing dry air (100 cm<sup>3</sup> min<sup>-1</sup>, Airgas, Ultra-zero grade) with the intent to remove residual volatiles and any organic species and to produce Si- $\beta$  (Si:Al > 1200, determined by ICP-OES).

Ti atoms were incorporated into the framework by liquid-phase incorporation (LPI),<sup>15,39,40</sup> which involved stirring Si- $\beta$  in dichloromethane (DCM, Fisher Chemicals, Certified ACS Stabilized, 15 cm<sup>3</sup> DCM g<sub>zeolite</sub><sup>-1</sup>) under an argon atmosphere using standard schlenk technique. An appropriate amount of TiCl<sub>4</sub> (Sigma-Aldrich, 99.9%) was added dropwise to the stirring suspension of Si- $\beta$  in DCM and brought to reflux (323 K) for 3 hours. Notably, TiCl<sub>4</sub> will violently react with moisture in air to release HCl, and should be handled carefully in an inert atmosphere. After ca. 30 minutes at reflux, the color of the suspension turned from bleached white to tan.

Nb and Ta atoms were also incorporated into the framework by LPI,<sup>15,39,40</sup> which involved stirring Si- $\beta$  in isopropanol (IPA, Fisher Chemicals, 15 cm<sup>3</sup> IPA g<sub>zeolite</sub><sup>-1</sup>) under an ambient atmosphere. An appropriate amount of NbCl<sub>5</sub> (Sigma-Aldrich, 99.9%) or TaCl<sub>5</sub> (Sigma-Aldrich, 99%) dissolved in IPA was added to the stirring suspension of Si- $\beta$  in IPA and heated to 333 K for 3 hours. Notably, NbCl<sub>5</sub> dissolved in IPA is bright yellow, and maintains this color for a short time (ca. 10 min) upon addition of Si- $\beta$ , after which the color of the suspension turns white.

For Ti-, Nb-, and Ta-samples, the solvent (i.e., DCM or IPA) was removed *in vacuo* (via rotovap), and the recovered solids were heated to 823 K at 5 K min<sup>-1</sup> for 6 h in flowing dry air (100 cm<sup>3</sup> min<sup>-1</sup>, Airgas, Ultra-zero grade). The heat-treated solids possessed a bleached white color.

Hf- and Zr-incorporated \*BEA materials were synthesized via solid-state ion exchange.<sup>38</sup> In brief, Si- $\beta$  was intimately ground with an appropriate amount of Hf(OEt)<sub>4</sub> (Alfa-Aesar, 99.9 %) or Zr(OEt)<sub>4</sub> (Alfa-Aesar, 99 %) to yield a homogeneous solid mixture. The solids were then heated to 823 K at 2 K min<sup>-1</sup> for 6 h in flowing air (100 cm<sup>3</sup> min<sup>-1</sup>, Airgas, Ultra-zero grade), with the intent to melt the Zr- and Hf(OEt)<sub>4</sub> and provide ample time for these species to diffuse into the SiOH pockets within the Si- $\beta$  crystals prior to decomposition. This process results in Zr- or Hf- $\beta$ , the colors of which are bleached white and light gray, respectively. This solid-state synthesis method can potentially produce extra-framework species (e.g., oligomeric ZrO<sub>x</sub> or HfO<sub>x</sub> species); however, characterization results (shown below) suggest the fraction of Zr- and Hf-

atoms that exist outside the framework are insignificant. Furthermore, the kinetic analysis (Sections 3.2 and S2) and correlations reported here rely only on how rates change with a function of reactant concentrations and temperature, such that an error in the site count would be systematically applied and would not alter any conclusions.

## 2.2 Catalyst Characterization

The transition metal content of each M- $\beta$  content was determined by inductively coupled plasma-optical emission spectroscopy (ICP-OES, PerkinElmer 2000DV), which was calibrated against known dilution standards. For M- $\beta$ , the subscript refers to the number of metal atoms per unit cell of the \*BEA framework, quantified by ICP-OES. For all kinetic and *in situ* spectroscopic measurements (Sections 2.3 and 2.4), samples of M- $\beta$  were prepared to result in 0.6 – 1 (M atoms)/(unit cell)<sup>-1</sup> (i.e., Si/M ratios > 60). Consequently, statistical arguments show that the M-atoms are well separated from one another and that catalysts will contain only a very small fraction of M-O-M linkages, which is supported also by other characterization methods described below. Furthermore, the post-synthetic modification of Al- $\beta$  only replaced approximately 1 in 5 Al atoms, which leaves ~4 silanol nests (unit cell)<sup>-1</sup>. This suggests that all M- $\beta$  used in this study are highly hydrophilic, rather than hydrophobic (as is the case in defectless M- $\beta$  materials).<sup>41</sup>

Catalyst crystallinity was confirmed by powder X-ray diffraction (p-XRD). X-ray diffractograms were obtained on a Siemens/Bruker D5000 diffractometer with Cu K- $\alpha$  radiation (0.15418 nm) using a step size of 0.02°, taken at 1° min<sup>-1</sup>, under ambient conditions. The similarities between the x-ray diffractograms (Fig. S1) show that the \*BEA framework remains intact after dealumination and metal incorporation for all M- $\beta$  samples.

Band edges ( $E_g$ ) were determined by analysis of diffuse reflectance UV-vis spectra of the bare M- $\beta$  materials (Fig. S2). Total reflectance spectra were measured at ambient conditions with a UV-vis-NIR spectrophotometer (Agilent CARY 5) equipped with a diffuse reflectance accessory (Harrick cricket®). Magnesium oxide (MgO, Sigma Aldrich, 99.995% trace metals basis) was used as a background for all spectra obtained. Samples were prepared by intimately combining M- $\beta$  (~10 mg) with MgO (~100 mg) using a pestle and mortar. Values of  $E_g$  were determined from the x-intercept of the linear portion of the corresponding Tauc plots for each material (Fig. S2b).<sup>42</sup> The relatively large value of the band edges (Table 1) for all of the materials (and absence of shoulders towards lower energies) further suggests that transition metal atoms within each of these materials are highly disperse and contain little to no oligomeric or bulk metal-oxide phases.<sup>17</sup>

The incorporation of the transition metal atoms into the \*BEA framework was confirmed by vibrational spectra of each sample obtained by attenuated total reflectance IR (ATR-IR) spectroscopy. Samples (~10 mg) were pressed onto the diamond internal reflection element of an ATR-IR instrument (Bruker Alpha) and spectra were recorded at ambient conditions (Fig. S3, 32 scans, 2 cm<sup>-1</sup> resolution). Figure S3a shows the normalized IR spectra for all M- $\beta$ , all of which possess nearly identical spectra within the framework stretching region. Figure S3b shows the difference spectra for group IV and V catalysts with respect to that of Si- $\beta$ , and are all normal-

ized to the well-documented  $\nu(\text{Si-O-M})$ <sup>15,43</sup> feature at 960 cm<sup>-1</sup>, for clarity. The appearance of this feature at ca. 960 cm<sup>-1</sup> ( $\nu(\text{Si-O-M})$ ) on all M- $\beta$  shows that the transition metal atoms are incorporated into the \*BEA framework upon post-synthetic modification.

The presence of Lewis acid sites was characterized by the IR spectra of adsorbed deuterated acetonitrile (CD<sub>3</sub>CN, Cambridge Isotope Laboratories, 99.8% D atom),<sup>44,45</sup> coordinated to M- $\beta$  using a custom-made transmission cell coupled to an FTIR spectrometer (Bruker, Tensor 37) equipped with a liquid-N<sub>2</sub>-cooled HgCdTe detector.<sup>46</sup> Catalysts were pressed into self-supporting wafers (~60 mg) and placed within the stainless-steel cell, which was equipped with CaF<sub>2</sub> windows and connected to a gas manifold by gas-transfer lines that were heated to 423 K via electrical heating tape (Omega, FGH Series). Catalysts were first heated to 423 K (10 K min<sup>-1</sup>) and held for 1.5 h under flowing He (50 cm<sup>3</sup> min<sup>-1</sup>, Airgas Ultra High Purity), with the intent to remove any residual H<sub>2</sub>O and other volatiles that may have adsorbed during catalyst storage. CD<sub>3</sub>CN was fed via a syringe pump (KD Scientific, Legato 100) at 1  $\mu\text{L min}^{-1}$  and vaporized inside the heated gas-transfer lines into a stream of flowing He (50 cm<sup>3</sup> min<sup>-1</sup>, Airgas, 99.999%) to produce a stream containing 1.0 kPa CD<sub>3</sub>CN. IR spectra (Fig. S4) of adsorbed CD<sub>3</sub>CN were obtained by flowing the CD<sub>3</sub>CN/He stream over the sample for 15 minutes. The flow of CD<sub>3</sub>CN was then stopped and the sample was heated at 10 K min<sup>-1</sup> to a final temperature of 423 K while FTIR spectra (128 scans, 1 cm<sup>-1</sup> resolution) were continuously recorded.

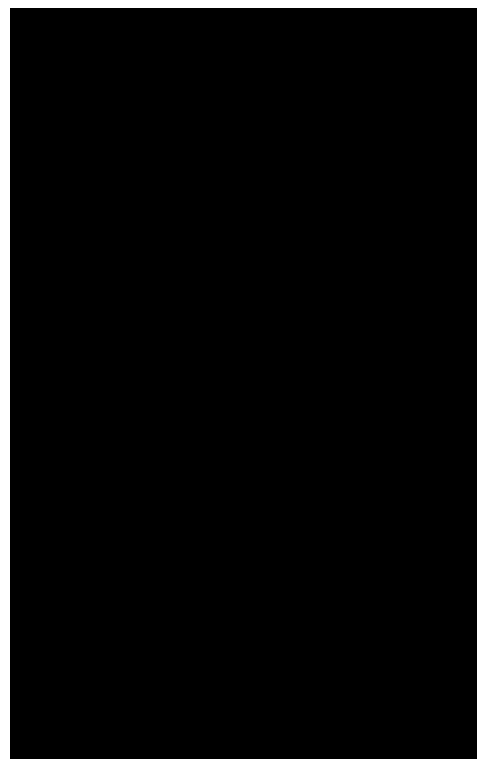


**Figure 1.** Infrared spectra of CD<sub>3</sub>CN bound to Lewis acid, Brønsted acid, and silanol sites on M- $\beta$  catalysts including Ti<sub>1.0</sub>- (blue), Zr<sub>1.0</sub>- (red), Hf<sub>1.0</sub>- (green), Nb<sub>0.2</sub>- (black), and Ta<sub>0.6</sub>- $\beta$  (orange). Spectra are normalized to  $\nu(\text{C}\equiv\text{N})$  of silanol-bound CD<sub>3</sub>CN (2274 cm<sup>-1</sup>) and were acquired in flowing He (50 cm<sup>3</sup> min<sup>-1</sup>, ~373 K) to monitor the desorption of CD<sub>3</sub>CN after saturation.



Figure 1 shows FTIR spectra for adsorbed CD<sub>3</sub>CN on all M- $\beta$  during the desorption of CD<sub>3</sub>CN in flowing He (50 cm<sup>3</sup> min<sup>-1</sup>, ~333 K) after saturation of CD<sub>3</sub>CN to visualize relevant CD<sub>3</sub>CN IR features. All M- $\beta$  possess an absorbance feature at ~2274 cm<sup>-1</sup>, which corresponds to  $\nu(\text{C}\equiv\text{N})$  of CD<sub>3</sub>CN coordinated to SiOH functionalities within the \*BEA framework. Ti-, Nb-, and Ta- $\beta$  each possess a single additional feature at 2302, 2306, and 2312 cm<sup>-1</sup>, respectively, which is assigned to  $\nu(\text{C}\equiv\text{N})$  of Lewis-acid bound CD<sub>3</sub>CN.<sup>41</sup> Both Zr- and Hf- $\beta$  possess two additional features at 2326 cm<sup>-1</sup> and 2296 cm<sup>-1</sup>. Of these two features, the peaks at 2296 cm<sup>-1</sup> are assigned to CD<sub>3</sub>CN coordinated to the Lewis acidic Zr and Hf atoms in the \*BEA framework, based on recent reports for Zr- $\beta$ .<sup>47</sup> Finally, CD<sub>3</sub>CN bound to Brønsted acid sites on H-exchanged USY<sup>48</sup> has been observed at 2332 cm<sup>-1</sup>; therefore, the features at 2326 cm<sup>-1</sup> on Zr- and Hf- $\beta$  may be attributed to CD<sub>3</sub>CN coordinated to Brønsted acid sites (e.g., (SiO)<sub>3</sub>Zr(OH)), as Zr- $\beta$  is known to contain Brønsted acid sites at open Zr sites in the framework.<sup>49</sup> Notably, the features at 2326 and 2296 cm<sup>-1</sup> in Zr- and Hf- $\beta$  do not correspond to remaining Lewis or Brønsted acidic Al atoms in the framework<sup>41</sup> as these features are not observed in the purely Si- $\beta$  starting material (Fig. S4), nor are they attributed to bulk or oligomeric extraframework metal oxide clusters.<sup>45</sup>

The presence and ratio of open versus closed sites has been shown to influence the reactivity of similar M- $\beta$  catalysts. For example, the rates for the conversion of ethanol to butadiene on Zr- $\beta$  has been shown to be proportional to the number of open Zr sites on a series of materials (as detected by FTIR of adsorbed CO at 100 K),<sup>50</sup> which suggests that butadiene forms primarily on open sites. Gounder and coworkers have used the FTIR spectra of adsorbed CD<sub>3</sub>CN to show that Sn- $\beta$  made by both post-synthetic modification and hydrothermal syntheses contain significant amounts of both open and closed sites, which suggests that it is extremely difficult to synthesize materials that contain solely one type of site.<sup>41</sup> Thus, the M- $\beta$  materials in this study likely contain a mixture of open and closed sites. However, the relationships developed within this work seek to correlate the experimentally observed reactivity (e.g., quantified by values of the  $\Delta H^\ddagger$  which do not depend on the number of sites) of these materials with a functional descriptor of the Lewis acid strength, rather than compare within each material the reactivity of open versus closed sites. Future studies will explore how changes in the prevalence of open or closed sites (e.g., manipulated using hydrothermal synthesis versus post-synthetic modification methods) affect the Lewis acid strength, reactivity, and selectivity of a given group IV or V metal in the framework of these zeolitic materials.

To obtain functional measures of the Lewis acid strength, the enthalpies for adsorption of CD<sub>3</sub>CN to Lewis acid sites ( $\Delta H_{\text{CD}_3\text{CN}}$ ) were determined by monitoring the absorbance value of the  $\nu(\text{C}\equiv\text{N})$  feature as a function of inverse temperature (at a constant partial pressure of CD<sub>3</sub>CN (Fig. S5, ~1.2 kPa CD<sub>3</sub>CN, 373 – 423 K). The coverage of Lewis-acid bound CD<sub>3</sub>CN is proportional to the intensity of the  $\nu(\text{C}\equiv\text{N})$  feature in the absorbance spectra, and the heat of adsorption for CD<sub>3</sub>CN onto Lewis-acid sites on each of the M- $\beta$  materials is calculated by the method of van't Hoff (Fig. S5). Table 1 summarizes the experimentally determined values of  $\Delta H_{\text{CD}_3\text{CN}}$  for all M- $\beta$  catalysts.

Overall, the results from p-XRD, diffuse reflectance UV-vis spectroscopy, and IR spectra of M<sub>x</sub>- $\beta$  and adsorbed CD<sub>3</sub>CN

show that the \*BEA framework is intact after post-synthetic modification; very little, if any, oligomeric or bulk metal oxide is present; metal atoms are incorporated into the framework; and quantify Lewis-acid strength, respectively (SI, Section S1; Table 1; Fig. 1 and S1 – S5).

**Table 1.** Heats of adsorption for CD<sub>3</sub>CN coordinated to Lewis acidic framework metal atoms and band edge energies (measured via DR UV-vis) for Nb<sub>0.6</sub>-, Ta<sub>0.6</sub>-, Ti<sub>1.0</sub>-, Zr<sub>1.0</sub>-, and Hf<sub>1.0</sub>- $\beta$ .

Sample	$\Delta H_{\text{CD}_3\text{CN}}$ (kJ mol <sup>-1</sup> )	Band Edge (eV)
Nb <sub>0.6</sub> - $\beta$	-22 $\pm$ 2	4.2
Ta <sub>0.6</sub> - $\beta$	-17 $\pm$ 1	4.8
Ti <sub>1.0</sub> - $\beta$	-31 $\pm$ 2	4.0
Zr <sub>1.0</sub> - $\beta$	-14 $\pm$ 1	5.6
Hf <sub>1.0</sub> - $\beta$	-13 $\pm$ 1	5.7

### 2.3 Measurements of Reaction Rates and Selectivities

Rates for cyclohexene (C<sub>6</sub>H<sub>10</sub>) epoxidation and H<sub>2</sub>O<sub>2</sub> decomposition were measured within batch reactors (100 cm<sup>3</sup>, three-neck round bottom flask) equipped with reflux condensers to minimize evaporative losses. Appropriate amounts of C<sub>6</sub>H<sub>10</sub> (Sigma-Aldrich, 99%) or *cis*-stilbene (Sigma-Aldrich, >96 %) and H<sub>2</sub>O<sub>2</sub> (Fischer Chemicals, 30 wt. % in H<sub>2</sub>O) were added to a solution of acetonitrile (CH<sub>3</sub>CN, Macron Chemicals, >99.8%) and benzene (for use as an internal standard, Sigma-Aldrich, thiophene free, >99%) and heated to the desired temperature (303 – 348 K) while stirring at 600 rpm. Epoxidation and H<sub>2</sub>O<sub>2</sub> decomposition was initiated by adding the M- $\beta$  catalyst. Small aliquots (~300  $\mu$ L) of the reaction solution were extracted as a function of time through a 0.22  $\mu$ m syringe filter (with the intent to remove suspended catalyst and quench epoxidation and H<sub>2</sub>O<sub>2</sub> decomposition). The hydrocarbon and oxygenate concentrations within these aliquots were quantified via a gas chromatograph (HP-5890, Series A) equipped with a flame-ionization detector. All species were identified and calibration factors were quantified using standards of known concentration. The H<sub>2</sub>O<sub>2</sub> concentration of each aliquot was determined by colorimetric titration using an aqueous solution of CuSO<sub>4</sub> (8.3 mM, Fisher Chemicals, >98.6%), neocuproine (12 mM, Sigma-Aldrich, >98%), and ethanol (25% v/v, Decon Laboratories Inc., 100%). The concentration of H<sub>2</sub>O<sub>2</sub> was quantified from comparison of the absorbance at 454 nm to calibrated standards, measured using a visible-light spectrophotometer (Spectronic, 20 Genesys). Test reactions (0.01 M C<sub>6</sub>H<sub>10</sub>, 1 mM H<sub>2</sub>O<sub>2</sub>, 313 K) with Si- $\beta$  reveal that no reaction (i.e., C<sub>6</sub>H<sub>10</sub> epoxidation or H<sub>2</sub>O<sub>2</sub> decomposition) occurs in the absence of the metal atoms. In all reported data, the carbon balance closed within 98% and the standard uncertainty for measured reaction rates was < 7%. Rates for the conversion of C<sub>6</sub>H<sub>10</sub> and H<sub>2</sub>O<sub>2</sub> on the five M- $\beta$  were measured as functions of [H<sub>2</sub>O<sub>2</sub>], [C<sub>6</sub>H<sub>10</sub>], and [C<sub>6</sub>H<sub>10</sub>O], and all reported results were obtained at differential conversion (i.e., < 5% conversion of limiting reagent).

Reported rates were measured in the absence of intra-pellet mass-transfer limitations, as shown by satisfying the Madon-Boudart criterion for Ti- $\beta$  (i.e., the M- $\beta$  catalyst with the greatest turnover rates) by performing reactions under identical conditions with catalysts containing different metal loadings (see SI, Section S1.2).<sup>51</sup> Over the metal loadings tested,

the epoxidation turnover rates did not depend on the metal content, which demonstrates that concentration gradients do not exist within the reactor or within the M- $\beta$  particles. Additionally, all catalysts tested are of similar metal loadings (group IV  $\sim 1$  (M atom)(unit cell) $^{-1}$ ; group V  $\sim 0.6$  (M atom)(unit cell) $^{-1}$ ).

#### 2.4 *In situ* UV-vis spectroscopy

*In situ* UV-vis spectroscopy was used to identify the intermediates formed upon  $\text{H}_2\text{O}_2$  activation and determine which of these species were directly responsible for olefin epoxidation. M- $\beta$  samples were pressed into 7 mm diameter pellets ( $\sim 5$  mg) and loaded into a custom-built UV-vis liquid flow cell equipped with cartridge heaters for temperature control. UV-vis spectra (100 scans, 600 ms integration time) were collected using a 45-degree diffuse reflection probe (Avantes, solarization-resistant fibers) connected to a fiber-optic spectrometer (Avantes, AvaFast 2048) with a compact deuterium-halogen light source (Avantes, AvaLight-DHc). Reactant and solvent solutions were introduced via a high-performance liquid chromatography pump (Waters, 515). A  $\text{CH}_3\text{CN}$  solution (0.4 M  $\text{H}_2\text{O}$ , 1  $\text{cm}^3 \text{min}^{-1}$ ) flowed over the samples at 313 K for 1 hr, and the corresponding UV-vis spectra for each M- $\beta$  was used as the background for all measurements. The M- $\beta$  samples were activated with  $\text{H}_2\text{O}_2$  by switching the flow to a solution of  $\text{H}_2\text{O}_2$  in  $\text{CH}_3\text{CN}$  (0.1 M  $\text{H}_2\text{O}_2$ , 0.4 M  $\text{H}_2\text{O}$ , 1  $\text{cm}^3 \text{min}^{-1}$ ) at 313 K until the UV-vis spectra became constant (i.e., implying a constant coverage of surface intermediates). Pure  $\text{CH}_3\text{CN}$  (1  $\text{cm}^3 \text{min}^{-1}$ ) was then flowed over the samples at 313 K for 10 min to remove residual  $\text{H}_2\text{O}_2$ . The reactivity of the surface intermediates was determined by continuously acquiring UV-vis spectra while flowing a solution of  $\text{C}_6\text{H}_{10}$  in  $\text{CH}_3\text{CN}$  (0.1 M  $\text{C}_6\text{H}_{10}$ , 0.4 M  $\text{H}_2\text{O}$ , 1  $\text{cm}^3 \text{min}^{-1}$ ) and by mathematically modeling the rates of peak attenuation (see SI, Section S2). Notably, separate experiments showed that the UV-vis absorbance features on the  $\text{H}_2\text{O}_2$ -activated M- $\beta$  did not change or attenuate (for a period of 2 hr) under a flowing stream of  $\text{CH}_3\text{CN}$  (0.4 M  $\text{H}_2\text{O}$ , 1  $\text{cm}^3 \text{min}^{-1}$ ) or pure  $\text{H}_2\text{O}$  (1  $\text{cm}^3 \text{min}^{-1}$ , 17.8 M $\Omega$ ) at 313 K. Processes for peak smoothing, background subtraction, and peak fitting were performed within OriginPro® and are described in the SI (Section S2).

### 3.0 RESULTS AND DISCUSSION

#### 3.1 Identifying Active Oxygen Intermediates for Epoxidations

Metal-bound superoxide ( $\text{M}-(\text{O}_2)^{\cdot -}$ ),<sup>15,52</sup> peroxide ( $\text{M}-(\text{O}_2)^{2-}$ ),<sup>16,20,24</sup> and hydroperoxide ( $\text{M}-\text{OOH}$ )<sup>24-26,53-55</sup> intermediates have been proposed as the active intermediates for olefin epoxidation on group IV and V catalysts grafted onto  $\text{SiO}_2$  and incorporated into zeolite frameworks. However, published results disagree over the exact identity of the reactive intermediate on these solid catalysts. The activation of  $\text{H}_2\text{O}_2$  on group IV (i.e., Ti, Zr, and Hf) and V (i.e., Nb and Ta) transition metal atoms incorporated into the \*BEA framework (M- $\beta$ ) likely forms a pool of superoxide, peroxide, and hydroperoxide intermediates, where these complexes may be characterized by their electronic transitions (e.g., ligand-to-metal charge transfer) via UV-vis spectroscopy.

UV-vis spectra of  $\text{H}_2\text{O}_2$ -activated M- $\beta$  acquired *in situ* (Fig. 2, 0.1 M  $\text{H}_2\text{O}_2$ , 0.4 M  $\text{H}_2\text{O}$ , in  $\text{CH}_3\text{CN}$ , 1  $\text{cm}^3 \text{min}^{-1}$ , 313 K) show that all M- $\beta$  materials possess overlapping absorbance

features (Fig. S8), whose intensities are proportional to the relative surface coverage of these species. Similar overlapping features exist on TS-1,<sup>24,56,57</sup> Nb- $\beta$ ,<sup>15</sup> and bulk  $\text{Nb}_2\text{O}_5$ ,<sup>58</sup> where the lower energy (higher wavelength ( $\lambda$ )) features are known to correspond to  $\text{M}-\text{OOH}/\text{M}-(\text{O}_2)^{2-}$  species while the higher energy (lower  $\lambda$ ) peaks are assigned to the  $\text{M}-(\text{O}_2)^{\cdot -}$  species.<sup>15,24,52,58,59</sup> As such, we systematically assign the higher  $\lambda$  features in Ta-, Zr-, and Hf- $\beta$  to the  $\text{M}-\text{OOH}/-(\text{O}_2)^{2-}$  species and the lower  $\lambda$  feature to  $\text{M}-(\text{O}_2)^{\cdot -}$ .

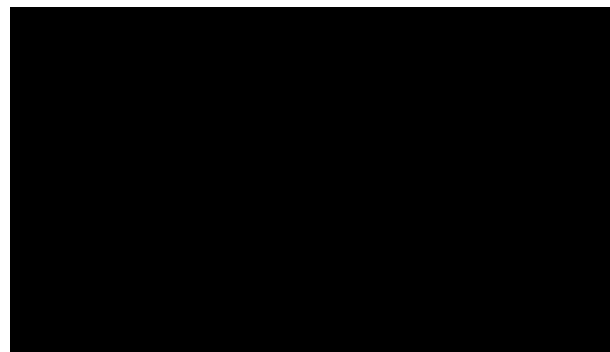
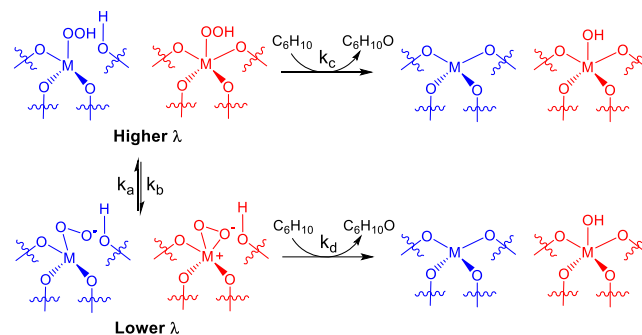


**Figure 2.** UV-vis spectra of  $\text{H}_2\text{O}_2$ -activated (Section 2.4) M- $\beta$  catalysts including Hf<sub>1.0</sub>- (green), Zr<sub>1.0</sub>- (red), Ta<sub>0.6</sub>- (orange), Nb<sub>0.2</sub>- (black), and Ti<sub>1.0</sub>- $\beta$  (blue). Spectra were acquired *in situ* in flowing  $\text{H}_2\text{O}_2$  in  $\text{CH}_3\text{CN}$  (0.1 M  $\text{H}_2\text{O}_2$ , 0.4 M  $\text{H}_2\text{O}$ , 1  $\text{cm}^3 \text{min}^{-1}$ ) at 313 K. Nb<sub>0.2</sub>- $\beta$  data is adapted from Ref [15].



**Scheme 1.** Interconversion and consumption of  $\text{M}-\text{OOH}/\text{M}-(\text{O}_2)^{2-}$  ( $\text{M}-\text{OOH}$  shown) and  $\text{M}-(\text{O}_2)^{\cdot -}$  species upon reaction with  $\text{C}_6\text{H}_{10}$ . Color coding is for clarity: Group IV (Ti, Zr, and Hf, blue) and V (Nb and Ta, red).

Scheme 1 shows the possible reaction of both the  $\text{M}-\text{OOH}/-(\text{O}_2)^{2-}$  and  $\text{M}-(\text{O}_2)^{\cdot -}$  intermediates with  $\text{C}_6\text{H}_{10}$ , where the differences in the rates of consumption of these species in the presence of  $\text{C}_6\text{H}_{10}$  will reflect the relative reactivity of these intermediates. However, to accurately estimate values of rate constants for the reaction of dioxygen species with  $\text{C}_6\text{H}_{10}$  (i.e.,  $k_c$  and  $k_d$ ), the analysis must account for the interconversion of these species via reversible isomerization and charge transfer processes (Section S2.3 discusses how the interconversion of the two intermediates is accounted for during the transient kinetic analysis).<sup>15,60</sup>

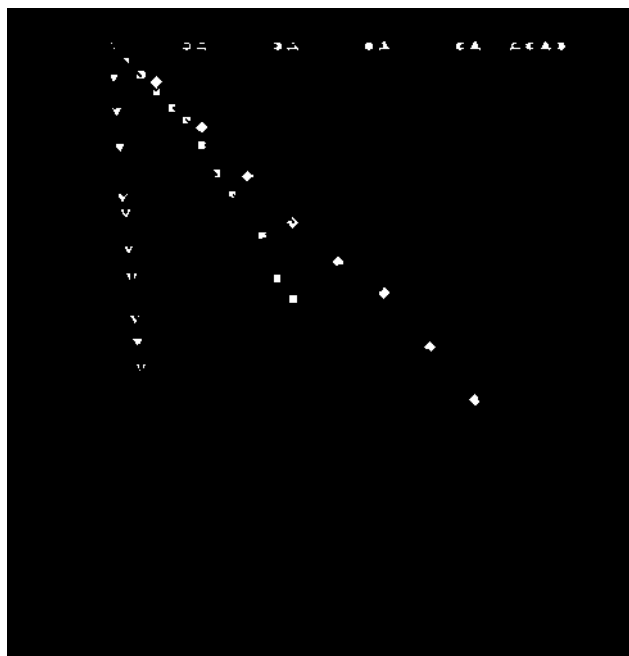


**Figure 3.** Change in the normalized surface coverage of M-OOH/M-(O<sub>2</sub>)<sup>2-</sup> (open symbols) and M-(O<sub>2</sub>)<sup>-</sup> (closed symbols) species as a function of time for Ti<sub>1.0</sub>-β (▼), Zr<sub>1.0</sub>-β (●), Hf<sub>1.0</sub>-β (▲), Nb<sub>0.2</sub>-β (■), and Ta<sub>0.6</sub>-β (◆). UV-vis spectra were acquired *in situ* upon flowing C<sub>6</sub>H<sub>10</sub> in CH<sub>3</sub>CN (0.1 M C<sub>6</sub>H<sub>10</sub>, 0.4 M H<sub>2</sub>O, 1 cm<sup>3</sup> min<sup>-1</sup>) over H<sub>2</sub>O<sub>2</sub>-activated samples (Section 2.4) at 313 K. Nb<sub>0.2</sub>-β data is adapted from Ref [15]. Closed symbols for Zr<sub>1.0</sub>-β and Hf<sub>1.0</sub>-β coincide with the open symbols. Note that the Y-axis is shown on a logarithmic scale.

The UV-vis absorbance features for species on Ti-, Nb-, and Ta-β attenuate exponentially with time upon exposure to flowing C<sub>6</sub>H<sub>10</sub> (0.1 M C<sub>6</sub>H<sub>10</sub>, 0.4 M H<sub>2</sub>O, in CH<sub>3</sub>CN, 313 K). Figure 3 shows the change in the normalized surface coverages of these species as a function of time and indicates clearly that specific intermediates are more reactive than others on a given M-β catalyst. Specifically, the number of Ti-OOH/(O<sub>2</sub>)<sup>2-</sup> species diminish at a faster rate than those for Ti-(O<sub>2</sub>)<sup>-</sup>, while the opposite is observed for Nb- and Ta-β. Table 2 shows rate constants for the reaction between M-(O<sub>2</sub>)<sup>-</sup> or M-OOH/(O<sub>2</sub>)<sup>2-</sup> intermediates and C<sub>6</sub>H<sub>10</sub> (Scheme 1) on each catalyst that are calculated from the change in the normalized intensity of the corresponding spectral features for each species (Fig. 3), during the reaction of H<sub>2</sub>O<sub>2</sub>-activated M-β with flowing C<sub>6</sub>H<sub>10</sub> at conditions similar to those for rate measurements (SI, Section S2.3). The calculated rate constants (Tables 2 and S2) for epoxidation by M-(O<sub>2</sub>)<sup>-</sup> on Nb- and Ta-β are 2·10<sup>4</sup> and 32 times larger than for epoxidation by M-OOH/(O<sub>2</sub>)<sup>2-</sup>, respectively, which suggests that superoxide species are the active intermediates for epoxidation on group V substituents in the \*BEA.<sup>15</sup> However, for Ti-β, the rate constant for the consumption of Ti-OOH/(O<sub>2</sub>)<sup>2-</sup> (i.e., k<sub>c</sub>) is larger than that for Ti-(O<sub>2</sub>)<sup>-</sup> (i.e., k<sub>d</sub>) by a factor of 170. This difference shows that the Ti-OOH/(O<sub>2</sub>)<sup>2-</sup> species are primarily responsible for olefin epoxidation on Ti-β, which agrees with the intermediates proposed for epoxidation reactions on TS-1.<sup>25,26,57,60,61</sup> The attenuation of the UV-vis absorbance features for Zr- and Hf-β were negligible on the time scale of the experiment, which corresponds to rate constants for epoxidation with these intermediates of < 10<sup>-6</sup> s<sup>-1</sup> and is consistent with kinetic measurements for these ma-

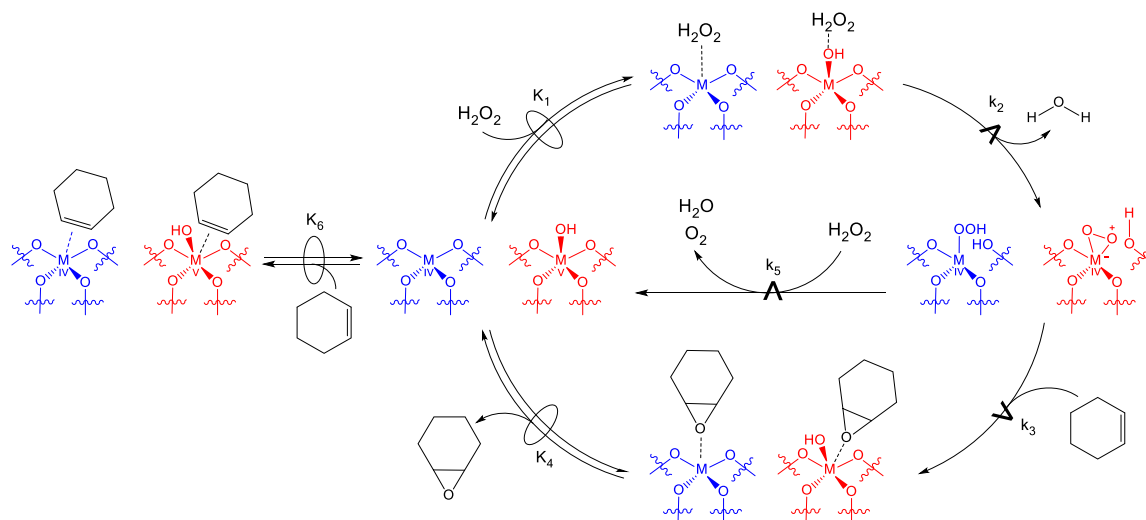
terials (i.e., the rates of reaction for Zr- and Hf-β are a factor of ~10<sup>5</sup> less than Ti-β at comparable conditions (Fig. 5)). The values of k<sub>c</sub> and k<sub>d</sub> could not be determined on Zr-β and Hf-β, because the attenuation rates were immeasurable, however, the identities of the H<sub>2</sub>O<sub>2</sub>-derived intermediates responsible for epoxidation on these materials was determined using an alternative method, described next.

Epoxidation reactions with Z-stilbene were used to support the identifications of the active intermediates derived from the *in situ* UV-vis measurements. Olefin epoxidations that involve M-OOH/(O<sub>2</sub>)<sup>2-</sup> species occur through a concerted mechanism, where oxygen-atom transfer from the active intermediate to the olefin occurs in a single step and, thus, prevents stereochemical rearrangement (e.g., C-C bond rotation).<sup>4,26,62</sup> Such epoxidations result in the nearly-exclusive formation of Z-stilbene oxide. Epoxidations that use M-(O<sub>2</sub>)<sup>-</sup> intermediates, however, react through a biradical mechanism that allows nearly unhindered rotation about the C=C bond, and therefore, gives distributions of epoxide products that contain comparable amounts of E- and Z-stilbene oxide isomers.<sup>15,63,64</sup> Table 2 shows that group IV (i.e., Ti, Zr, and Hf) catalysts preferentially form Z-stilbene oxide, while group V (i.e., Nb and Ta) produce nearly equal amounts of Z- and E-stilbene oxide. The microporous nature of these materials does not introduce artifacts in the analysis or the interpretation of these isomer distributions. The disparity in the Z:E ratio of stilbene oxide between group IV and V metals (Table 2), suggests that the pore geometry has minimal, if any, effect on the distribution of products. An *in situ* UV-vis experiment was performed on H<sub>2</sub>O<sub>2</sub>-activated Ti-β (Fig. S9) to determine if Z-stilbene was able to diffuse into the \*BEA framework and react with all Ti-atoms within the bulk. The absorbance features for both M-OOH/(O<sub>2</sub>)<sup>2-</sup> and M-(O<sub>2</sub>)<sup>-</sup> attenuated exponentially and indicate that ~95 % of the intermediates were consumed, which strongly suggests that the Z-stilbene is able to fully access the pores of M-β and react. Consequently, the E- and Z-stilbene oxide isomers form by reactions that occur on the same sites and with the same intermediates that facilitate C<sub>6</sub>H<sub>10</sub> epoxidation and not on a subset of sites on the exterior surface of the catalyst particles. These product isomer distributions, in conjunction with *in situ* UV-vis measurements (Fig. 3) and the calculated rate constants (Table 2), strongly suggest that the reactive intermediate(s) responsible for olefin epoxidation on group IV (i.e., Ti, Zr, and Hf) catalysts are the M-OOH/(O<sub>2</sub>)<sup>2-</sup> species, while group V (i.e., Nb and Ta) materials react through a M-(O<sub>2</sub>)<sup>-</sup> intermediate.

**Table 2.** Evidence for the Direct Involvement of Specific Intermediates in Olefin Epoxidation: Rate constants for the epoxidation of C<sub>6</sub>H<sub>10</sub> and Z:E (*cis:trans*) stilbene oxide product ratios for the epoxidation of Z-stilbene

Sample	k <sub>c</sub> (s <sup>-1</sup> )	k <sub>d</sub> (s <sup>-1</sup> )	Z:E ratio
Ti <sub>1.0</sub> -β	2.9·10 <sup>-2</sup>	1.7·10 <sup>-4</sup>	9.2
Nb <sub>0.2</sub> -β	2.2·10 <sup>-7</sup>	4.5·10 <sup>-3</sup>	1.0
Ta <sub>0.6</sub> -β	1.0·10 <sup>-4</sup>	3.3·10 <sup>-3</sup>	1.0
Zr <sub>1.0</sub> -β	< 10 <sup>-6</sup>	< 10 <sup>-6</sup>	7.1
Hf <sub>1.0</sub> -β	< 10 <sup>-6</sup>	< 10 <sup>-6</sup>	6.3

**Figure 4.** Turnover rates for the formation of  $C_6H_{10}O$  as a function of (a)  $C_6H_{10}$  over  $Nb_{0.6}\beta$  (■, 1 mM  $H_2O_2$ , 313 K),  $Ta_{0.6}\beta$  (◆, 1 mM  $H_2O_2$ , 313 K),  $Ti_{1.0}\beta$  (▼, 0.01 M  $H_2O_2$ , 313 K),  $Zr_{1.0}\beta$  (●, 0.1 M  $H_2O_2$ , 323 K), and  $Hf_{1.0}\beta$  (▲, 0.1 M  $H_2O_2$ , 323 K), (b)  $H_2O_2$  over  $Nb_{0.6}\beta$  (□, 0.05 M  $C_6H_{10}$ , ■, 3 M  $C_6H_{10}$ , 313 K),  $Ta_{0.6}\beta$  (◇, 2 mM  $C_6H_{10}$ , ◆, 0.5 M  $C_6H_{10}$ , 313 K),  $Ti_{1.0}\beta$  (▽, 0.05 M  $C_6H_{10}$ , ▼, 0.5 M  $C_6H_{10}$ , 313 K),  $Zr_{1.0}\beta$  (○, 5 mM  $C_6H_{10}$ , 323 K), and  $Hf_{1.0}\beta$  (△, 5 mM  $C_6H_{10}$ , 323 K), and (c)  $C_6H_{10}O$  over  $Nb_{0.6}\beta$  (■, 3 M  $C_6H_{10}$ , 1 mM  $H_2O_2$ , 313 K),  $Ta_{0.6}\beta$  (◆, 0.5 M  $C_6H_{10}$ , 1 mM  $H_2O_2$ , 313 K),  $Ti_{1.0}\beta$  (▼, 0.5 M  $C_6H_{10}$ , 0.01 M  $H_2O_2$ , 313 K). Dashed lines are intended to guide the eye. Nb- $\beta$  data is adapted from Ref [15].



**Scheme 2.** Proposed mechanism for the epoxidation of  $C_6H_{10}$  with  $H_2O_2$  over group IV (Ti, Zr, and Hf, M-OOH shown, blue) and group V (Nb and Ta, red) M- $\beta$ . The symbol ■ represents a quasi-equilibrated step, while ▼ represents a kinetically relevant step. Note, the unoccupied metal atoms are meant to be representations of an empty site, rather than suggest all metal atoms exist as closed sites, as both open and closed sites likely exist in these materials (see characterization results, Section 2.2).

### 3.2 Mechanistic Interpretation of Kinetic Data

Figure 4a shows turnover rates for the formation of cyclohexene oxide ( $C_6H_{10}O$ ) as a function of  $[C_6H_{10}]$  ( $10^{-4}$  – 5 M) at constant  $[H_2O_2]$  over all M- $\beta$ , while Fig. 4b shows turnover rates for  $C_6H_{10}O$  formation as a function of  $[H_2O_2]$  at constant  $[C_6H_{10}]$ , and Fig. 4c shows  $C_6H_{10}O$  formation rates as a function of  $[C_6H_{10}O]$  at constant  $[H_2O_2]$  and  $[C_6H_{10}]$ . In all cases,

rates of epoxidation depend linearly on  $[C_6H_{10}]$  (Fig. 4a) and do not depend on  $[H_2O_2]$  (Fig. 4b) at relatively low  $[C_6H_{10}]:[H_2O_2]$ , which suggests that the active sites are saturated with a  $H_2O_2$ -derived intermediate at these conditions. As  $[C_6H_{10}]:[H_2O_2]$  reactant ratios increase, the rate of epoxidation eventually becomes independent of  $[C_6H_{10}]$  (Fig. 4a), proportional to  $[H_2O_2]$  (Fig. 4b, Ti-, Nb-, and Ta- $\beta$ ), and inversely



proportional to  $[C_6H_{10}O]$  (Fig. 4c). This change suggests that the identity of the most abundant surface intermediate (MASI) changes to a  $C_6H_{10}$ -derived intermediate (e.g., most likely  $C_6H_{10}O$ ). Conceptually, this occurs because  $C_6H_{10}$  and its derivatives displace  $H_2O_2$ -derived species from the metal centers at high values of  $[C_6H_{10}]$ . Notably, the effect of  $[C_6H_{10}O]$  on epoxidation turnover rates on Zr- and Hf- $\beta$  (comparable to Fig. 4c) could not be measured because catalytic turnover rates at high  $[C_6H_{10}]$  ( $> 1$  M) were obscured by non-catalytic  $C_6H_{10}$  oxidation rates (i.e., homogeneous reactions).

Scheme 2 shows a series of elementary steps that account for the measured effects of  $[C_6H_{10}]$  (Fig. 4a),  $[H_2O_2]$  (Fig. 4b), and  $[C_6H_{10}O]$  (Fig. 4c) on both rates of  $C_6H_{10}$  epoxidation and of  $H_2O_2$  decomposition ( $H_2O_2$  decomposition rate expression is derived in SI, section S3.2).<sup>15</sup> The catalytic cycle for epoxidation involves the quasi-equilibrated adsorption of  $H_2O_2$  (step 1),<sup>15,16,51</sup> followed by the irreversible activation of  $H_2O_2$  (step 2) to form a pool of  $M-(O_2)^-$  and  $M-OOH/(O_2)^{2-}$  active intermediates (referred to collectively as  $M-(O_2)$ ).<sup>4,15,25,60,65</sup> Among these species, either  $M-OOH/(O_2)^{2-}$  or  $M-(O_2)^-$  then reacts with  $C_6H_{10}$  (depending on the metal identity, Section 3.1) via an Eley-Rideal mechanism to form  $C_6H_{10}O$  (step 3), which desorbs (step 4). The  $M-(O_2)$  species may also decompose nonproductively by reaction with  $H_2O_2$  (step 5). Measured  $C_6H_{10}$  epoxidation rates represent the kinetically relevant reaction of the active form of the oxidizing surface intermediate with a  $C_6H_{10}$  molecule:

$$r_E = k_3[M - O_2][C_6H_{10}] \quad (1)$$

where  $r_E$  is the rate of  $C_6H_{10}$  epoxidation,  $[M-(O_2)]$  is the number of the  $M-OOH/(O_2)^{2-}$  (group IV) or  $M-(O_2)^-$  (group V) species and  $k_x$  is the rate constant for step  $x$  in Scheme 2. Application of the pseudo-steady state hypothesis to the  $M-(O_2)$  intermediates, in combination with a site balance to account for all surface species (full derivation in SI, Section 3.1), provides:

$$\frac{r_E}{[L]} = \frac{k_2 k_3 K_1 [C_6H_{10}] [H_2O_2]}{(k_3 [C_6H_{10}] + k_5 [H_2O_2]) \beta} \quad (2)$$

where  $[L]$  is the total number of M atoms (i.e., active sites) present during reaction, and  $\beta$  describes the sum of terms representing all potential surface intermediates:

$$\beta = 1 + K_6 [C_6H_{10}] + K_1 [H_2O_2] + \frac{k_2 K_1 [H_2O_2]}{(k_3 [C_6H_{10}] + k_5 [H_2O_2])} + K_4 [C_6H_{10}O] \quad (3)$$

Here,  $K_x$  is the equilibrium constant for each step  $x$ , such that the five terms in  $\beta$  correspond to the number of site occupied by  $CH_3CN$  (i.e., the solvent),  $C_6H_{10}$ ,  $H_2O_2$ ,  $-(O_2)$  species, and  $C_6H_{10}O$ , respectively. At high  $[H_2O_2]:[C_6H_{10}]$  reactant ratios (e.g., 10 for Ti- $\beta$ ),  $M-(O_2)$  species become MASI, which

is shown by epoxidation rates that increase linearly with  $[C_6H_{10}]$  and do not depend on  $[H_2O_2]$  (Fig. 4). In this limit, equation 2 simplifies to the form:

$$\frac{r_E}{[L]} = k_3 [C_6H_{10}] \quad (4)$$

which is consistent with the measured dependence of  $r_E$  on the reactant concentrations (Fig. 4). Similarly, at lower ratios of  $[H_2O_2]:[C_6H_{10}]$ , the reaction product ( $C_6H_{10}O$ ) becomes the MASI as indicated by epoxidation rates that are independent of  $[C_6H_{10}]$  and proportional to  $[H_2O_2]$  (Fig. 4b), but also inversely dependent on  $[C_6H_{10}O]$  (Fig. 4c, observed on Ti-, Nb-, and Ta- $\beta$ ). When  $C_6H_{10}O$  is the MASI, the rate of epoxidation is much greater than the rate of  $H_2O_2$  decomposition (i.e.,  $k_3 [C_6H_{10}] \gg k_5 [H_2O_2]$ ; SI, Section S3.2), and, equation 2 simplifies to yield:

$$\frac{r_E}{[L]} = \frac{k_2 K_1 [H_2O_2]}{k_5 K_4 [C_6H_{10}O]} \quad (5)$$

Notably the form of equation 5 matches the ways in which  $r_E$  changes with variations in  $[C_6H_{10}]$  and  $[H_2O_2]$  as well as  $[C_6H_{10}O]$ .

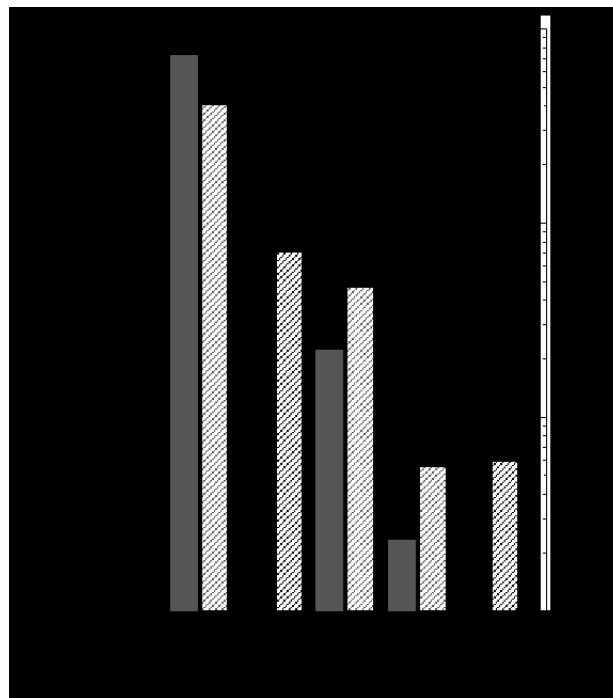


**Figure 5.** Turnover rates for the formation of  $C_6H_{10}O$  (solid) and  $H_2O_2$  selectivities (taken as the ratio of the turnover rate for  $C_6H_{10}O$  formation to total  $H_2O_2$  consumption, striped) for Ti<sub>1.0</sub>- $\beta$  (blue), Nb<sub>0.6</sub>- $\beta$  (black), Ta<sub>0.6</sub>- $\beta$  (orange), Zr<sub>1.0</sub>- $\beta$  (red), and Hf<sub>1.0</sub>- $\beta$  (green) (5 mM  $C_6H_{10}$ , 5 mM  $H_2O_2$ , at 313 K).

Figure 5 shows that these M- $\beta$  catalysts all have very different turnover rates and selectivities (i.e., productive use of  $\text{H}_2\text{O}_2$ ) at standardized conditions (5 mM  $\text{C}_6\text{H}_{10}$ , 5 mM  $\text{H}_2\text{O}_2$ , 313 K). For example, Ti- $\beta$  gives turnover rates that are a factor of  $10^5$  (i.e., 100,000) times greater and selectivities that are 60 times greater than those on Zr- $\beta$  (one element down group IV), while changing the metal from Nb to Ta results in minimal changes in rates and selectivities. Epoxidation rates depend on  $[\text{C}_6\text{H}_{10}]$ ,  $[\text{H}_2\text{O}_2]$ , and  $[\text{C}_6\text{H}_{10}\text{O}]$  in similar ways on all M- $\beta$ , which strongly suggests that these materials catalyze olefin epoxidation with  $\text{H}_2\text{O}_2$  through the common mechanism shown in Scheme 2. The reasons for such large differences in turnover rates and selectivities and the disparity between group IV and V catalysts must be related to consequential differences in the electronic structure and reactivity of the involved intermediates. Moreover, these differences must produce activation barriers for epoxidation and  $\text{H}_2\text{O}_2$  decomposition that depend on both the elemental identity and the details of how these transition metal atoms are coordinated within the \*BEA framework. Revealing the reasons for these differences requires both quantitative measurements of the activation barriers and methods to probe the chemical properties of the active sites and the electronic structure of the reactive intermediates that bind to these sites. To make equitable comparisons among activation barriers for epoxidation and  $\text{H}_2\text{O}_2$  decomposition reactions, all M- $\beta$  materials must be evaluated within the same kinetic regime (i.e., at comparable surface coverages, MASI).

**Table 3.** Activation enthalpies and entropies for  $\text{C}_6\text{H}_{10}$  epoxidation ( $\Delta H^\ddagger_{\text{E}}$  and  $\Delta S^\ddagger_{\text{E}}$ ) and  $\text{H}_2\text{O}_2$  decomposition ( $\Delta H^\ddagger_{\text{D}}$  and  $\Delta S^\ddagger_{\text{D}}$ ) over M- $\beta$  catalysts, measured on M-( $\text{O}_2$ ) saturated sites.

Sample	$\Delta H^\ddagger_{\text{E}}$ (kJ mol <sup>-1</sup> )	$\Delta S^\ddagger_{\text{E}}$ (J mol <sup>-1</sup> K <sup>-1</sup> )	$\Delta H^\ddagger_{\text{D}}$ (kJ mol <sup>-1</sup> )	$\Delta S^\ddagger_{\text{D}}$ (J mol <sup>-1</sup> K <sup>-1</sup> )
Nb <sub>0.6</sub> - $\beta$	72 $\pm$ 5	-35 $\pm$ 21	45 $\pm$ 5	-91 $\pm$ 30
Ta <sub>0.6</sub> - $\beta$	86 $\pm$ 6	-19 $\pm$ 11	56 $\pm$ 5	-61 $\pm$ 25
Ti <sub>1.0</sub> - $\beta$	43 $\pm$ 5	-53 $\pm$ 30	31 $\pm$ 10	-104 $\pm$ 40
Zr <sub>1.0</sub> - $\beta$	91 $\pm$ 10	-31 $\pm$ 9	65 $\pm$ 8	-55 $\pm$ 25
Hf <sub>1.0</sub> - $\beta$	93 $\pm$ 7	-26 $\pm$ 8	64 $\pm$ 6	-77 $\pm$ 21

Table 3 shows activation enthalpies ( $\Delta H^\ddagger$ ) and entropies ( $\Delta S^\ddagger$ ) for both  $\text{C}_6\text{H}_{10}$  epoxidation ( $\Delta H^\ddagger_{\text{E}}$  and  $\Delta S^\ddagger_{\text{E}}$ ) and  $\text{H}_2\text{O}_2$  decomposition ( $\Delta H^\ddagger_{\text{D}}$  and  $\Delta S^\ddagger_{\text{D}}$ ) obtained on M-( $\text{O}_2$ ) saturated surfaces (i.e., where rates are proportional to  $[\text{C}_6\text{H}_{10}]$  and independent of  $[\text{H}_2\text{O}_2]$  in Fig. 4) by operating at high  $[\text{H}_2\text{O}_2]:[\text{C}_6\text{H}_{10}]$  reactant ratios and by measuring rates of reaction as a function of inverse temperature (SI, Section S3.3, Fig. S11). Notably, values of  $\Delta S^\ddagger_{\text{E}}$  and  $\Delta S^\ddagger_{\text{D}}$  do not change systematically with the identity of the metal, because these activation entropies largely reflect the loss of translational entropy that results from the coordination of either  $\text{C}_6\text{H}_{10}$  or  $\text{H}_2\text{O}_2$  to the activated catalyst for epoxidation and  $\text{H}_2\text{O}_2$  decomposition pathways, respectively. Table 3 shows that values of  $\Delta H^\ddagger$  are much smaller for Ti- $\beta$  (the catalyst with the greatest turnover rates), somewhat larger for Nb- and Ta- $\beta$ , and  $\sim 50$  kJ mol<sup>-1</sup> greater on Zr- and Hf- $\beta$  (the catalysts with the lowest

turnover rates). Although these active site structures are similar in coordination (among Ti-, Hf-, and Zr- $\beta$ ), clearly the  $10^5$ -fold difference in rates (Fig. 5) and 50 kJ mol<sup>-1</sup> change in  $\Delta H^\ddagger_{\text{E}}$  must reflect some intrinsic property of the metal atom, how the metal coordinates to the framework, and properties of the M-( $\text{O}_2$ ) species (i.e., active intermediate).

Previous studies have attempted to relate the reactivity of site-isolated group IV and V metal atoms grafted onto mesoporous  $\text{SiO}_2$  to the Pauling electronegativity ( $E_x$ , where x represents the elemental identity) of the metal.<sup>23,66,67</sup> Values of  $\Delta H^\ddagger$  and  $E_x$  among the different M- $\beta$  catalysts appear to correlate linearly for Nb-, Ta-, Zr-, and Hf- $\beta$  and  $\Delta H^\ddagger$  values decrease with increasing electronegativity (Fig. S12); however, the values of  $\Delta H^\ddagger$  for both reactions (i.e.,  $\text{C}_6\text{H}_{10}$  epoxidation and  $\text{H}_2\text{O}_2$  decomposition) on Ti- $\beta$  are grossly overestimated (by 40 kJ mol<sup>-1</sup>) by this trend. The fact that  $E_x$  values alone are not enough to predict reactivity is not surprising, because the electronic structure of the metal sites and their Lewis acid strength should reflect, in part, their coordination environment within the zeolite framework. This same consideration also indicates that the  $E_x$  of the metal atoms should not be an accurate predictor for the properties of the active oxidizing intermediates (i.e., M-OOH/( $\text{O}_2$ )<sup>2-</sup> for group IV or M-( $\text{O}_2$ )<sup>-</sup> for group V). Therefore, a complete understanding of the role that metal identity has for epoxidation with  $\text{H}_2\text{O}_2$  requires a direct measurement of Lewis acid strength of the metal centers (as it exists in the zeolite framework) and the electronic structure of the reactive intermediate (acquired *in situ*).

### 3.3 Importance of Lewis Acid Strength and Electronic Structure for Olefin Epoxidations

The enthalpy of adsorption of  $\text{CD}_3\text{CN}$  ( $\Delta H_{\text{CD}_3\text{CN}}$ ) to Lewis acid sites provides a direct and quantitative measure of the Lewis acid strength for all M- $\beta$ . Values of  $\Delta H_{\text{CD}_3\text{CN}}$  were determined by van't Hoff analysis of  $\text{CD}_3\text{CN}$  adsorption isobars as a function of inverse temperature (Fig. S5, Table 1). These measurements were acquired using transmission infrared (IR) spectroscopy to quantify the change in the coverage of  $\text{CD}_3\text{CN}$  at individual Lewis acid sites (Section 2.2) by monitoring the intensity of the specific  $\nu(\text{C}\equiv\text{N})$  feature of interest within the range of 2295 – 2320 cm<sup>-1</sup>. This approach distinguishes between the amounts of  $\text{CD}_3\text{CN}$  adsorbed by physisorption to the zeolite framework, coordination to surface silanol groups, and strong chemisorption to Lewis acid sites, because each adsorption mode produces a distinct  $\nu(\text{C}\equiv\text{N})$  absorbance feature in the IR spectra (Fig. S4).<sup>35,44</sup> Consequently, IR spectroscopy allows measurements of  $\Delta H_{\text{CD}_3\text{CN}}$  at distinct Lewis acid sites, while conventional calorimetric methods would give ensemble averaged values that would lack specificity for  $\text{CD}_3\text{CN}$  molecules adsorbed to Lewis acid sites.

Figure 6a shows that values of  $\Delta H^\ddagger_{\text{E}}$  and  $\Delta H^\ddagger_{\text{D}}$  depend linearly on  $\Delta H_{\text{CD}_3\text{CN}}$  for all M- $\beta$  catalysts, which strongly suggests that stronger Lewis acids (i.e., more negative  $\Delta H_{\text{CD}_3\text{CN}}$ ) possess lower activation enthalpies for both  $\text{C}_6\text{H}_{10}$  epoxidation and  $\text{H}_2\text{O}_2$  decomposition. These trends show that stronger Lewis acid sites give greater turnover rates (Fig. 4 - 6), lower  $\Delta H^\ddagger$  values (Table 3), and greater selectivities for epoxidation (Fig. 5), because strong acids pull electron density away from the -( $\text{O}_2$ )<sup>-</sup> or -OOH/( $\text{O}_2$ )<sup>2-</sup> moiety, making these oxidants more electrophilic and reactive. Consequently, these surface

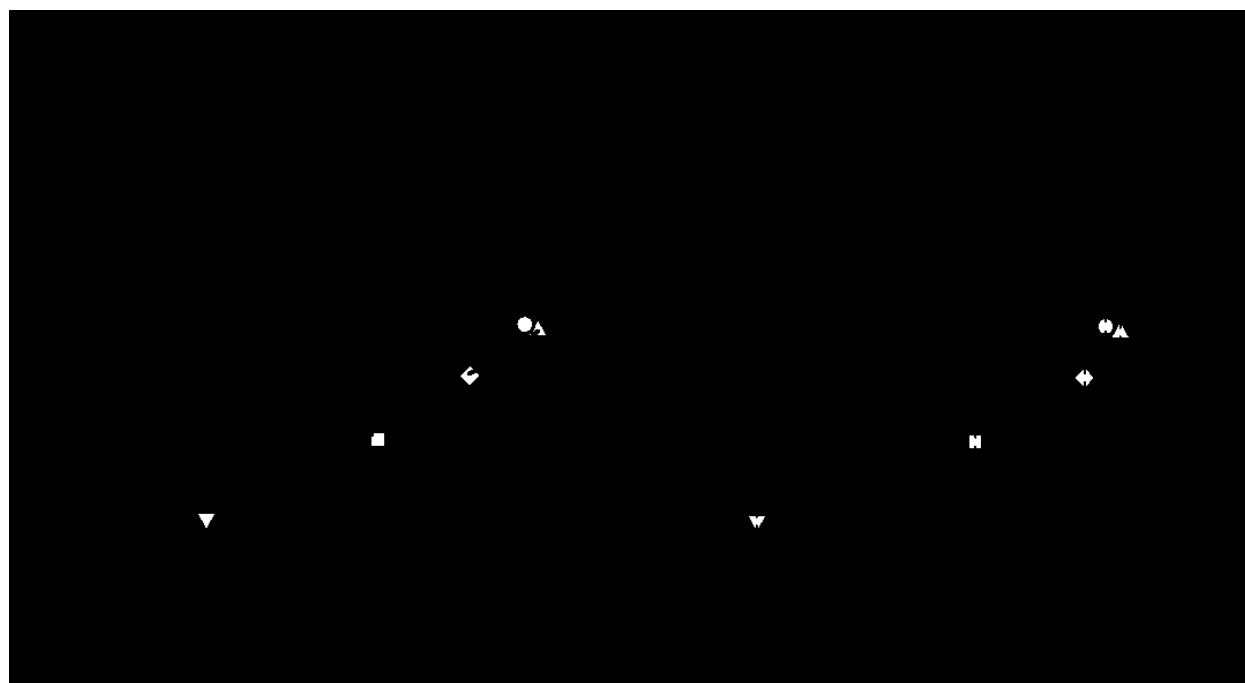


**Figure 6.** Comparisons between activation enthalpies for  $\text{C}_6\text{H}_{10}$  epoxidation ( $\Delta H^\ddagger_E$ , solid symbols) and  $\text{H}_2\text{O}_2$  decomposition ( $\Delta H^\ddagger_D$ , open symbols) for  $\text{M}-(\text{O}_2)$  saturated surfaces of  $\text{M}-\beta$  catalysts and measured (a) heats of adsorption for acetonitrile to the active sites ( $\Delta H^\ddagger_{\text{CD}_3\text{CN}}$ ; Table 1) and (b) ligand-to-metal charge transfer (LMCT) energies (Table S1) of the specific reactive intermediate identified on each catalyst for Ti- $\beta$  ( $\blacktriangledown$ ), Nb- $\beta$  ( $\blacksquare$ ), Ta- $\beta$  ( $\blacklozenge$ ), Zr- $\beta$  ( $\bullet$ ), and Hf- $\beta$  ( $\blacktriangle$ ). Dashed lines represent linear fits.

species are more reactive towards electron-rich functions of  $\text{C}_6\text{H}_{10}$  (i.e., the  $\text{C}=\text{C}$ ) and  $\text{H}_2\text{O}_2$  (i.e., the lone pairs of O).<sup>68</sup> The phenomena observed here was alluded to by Boronat *et al.*, who predicted that among Lewis acidic metal atoms within the \*BEA framework those with a lower-energy LUMO would give greater rates for the epoxidation of olefins.<sup>31</sup> Additionally, these experimentally determined descriptors of the Lewis acid strength (i.e.,  $\Delta H^\ddagger_{\text{CD}_3\text{CN}}$ ) and the electronic structure of the reactive intermediate (i.e., LMCT energy, discussed below (Fig. 6b)) also show the reasons for the large differences in selectivity for  $\text{H}_2\text{O}_2$  use in the epoxidations (discussed next). To the best of our knowledge, these data provide the first clear link between both the turnover rates and selectivities of  $\text{M}-\beta$  catalysts for epoxidation that span multiple groups in the periodic table and show how these catalytic properties depend on the Lewis acid strength of the active sites and also the electronic structure of the reactive species that are formed.

Furthermore, the difference in the slopes for  $\Delta H^\ddagger_E$  ( $\sim 3$ ) and  $\Delta H^\ddagger_D$  ( $\sim 2$ ) as a function of  $\Delta H^\ddagger_{\text{CD}_3\text{CN}}$ , show that the most electrophilic  $\text{M}-(\text{O}_2)$  intermediates give the greatest selectivities for epoxidation (Fig. 5), which is industrially desirable. Figure 5 shows that  $\text{H}_2\text{O}_2$  selectivities increase by nearly a factor of 60 at these conditions when the framework metal atom changes from Hf ( $\sim 0.5\%$ ) to Ti (38%). Note that different reaction conditions are used to optimize the  $\text{H}_2\text{O}_2$  selectivity on the most selective material (e.g., selectivities exceeding 95% for Ti- $\beta$  at high  $[\text{C}_6\text{H}_{10}]:[\text{H}_2\text{O}_2]$ ). For all  $\text{M}-\beta$ ,  $\text{C}_6\text{H}_{10}$  epoxidation (Section 3.2) and  $\text{H}_2\text{O}_2$  decomposition (SI, Section S3.2) occur through an Eley-Rideal mechanism between  $\text{C}_6\text{H}_{10}$  or  $\text{H}_2\text{O}_2$  with the active  $\text{M}-(\text{O}_2)$  intermediate,<sup>15,54</sup> which when combined with the observed dependencies of  $\Delta H^\ddagger_E$  and  $\Delta H^\ddagger_D$  on  $\Delta H^\ddagger_{\text{CD}_3\text{CN}}$  suggests that there is a stronger interaction of  $\text{C}_6\text{H}_{10}$

with the  $\text{M}-(\text{O}_2)$  specie than  $\text{H}_2\text{O}_2$  in the transition state. This trends differs from previously proposed O-O bond homolysis mechanism for  $\text{H}_2\text{O}_2$  decomposition over TS-1,<sup>56,69</sup> where increasing Lewis acid strength was thought to decrease  $\text{H}_2\text{O}_2$  decomposition rates by pulling electron density from the  $-(\text{O}_2)$  moiety and, thus, decreases the propensity for O-O bond cleavage. The data and conclusions here (i.e., Fig. 6, more electrophilic intermediates yield greater epoxidation rates) are consistent with the prior observation that epoxidation turnover rates increase with the electron richness of the olefin (e.g., allyl alcohol > allyl chloride > 1-hexene).<sup>4,26</sup> Importantly, here the electronic structure of the active site was modified (and by extension the structure and form of the reactive dioxygen intermediate that is active for epoxidation) by changing the identity of the transition metal substituent, whereas, the earlier studies manipulated rates by changing the structure of the reactant.

Figure 6b shows that  $\Delta H^\ddagger_E$  and  $\Delta H^\ddagger_D$  also increase linearly with the energy for LMCT (assessed by UV-vis) for the active intermediate (i.e., specifically  $\text{M}-(\text{O}_2)^\cdot$  species for group V and  $\text{M}-\text{OOH}/-(\text{O}_2)^{2-}$  for group IV, Fig. 2 and S8) on all  $\text{M}-\beta$ . Higher LMCT energies reflect weaker Lewis acid sites, because these catalysts have a lower tendency to pull electron density towards the metal nuclei. As such, electronic transitions in weaker Lewis acids (e.g., Hf) require higher-energy photons, as the electrons have the preference to reside on the  $-\text{OOH}/-(\text{O}_2)^{2-}$  or  $-(\text{O}_2)^\cdot$  moiety. Conversely, a strong Lewis acid (i.e., Ti) has the tendency to pull electron density to the metal center, resulting in a lower energy LMCT as there is a smaller energetic preference for the electrons to reside on the  $-\text{OOH}/-(\text{O}_2)^{2-}$  or  $-(\text{O}_2)^\cdot$ . These differences correlate with the  $\Delta H^\ddagger_E$  and  $\Delta H^\ddagger_D$  values and show that the  $\text{M}-\text{O}_2$  species with the greatest

degree of electrophilicity are the most reactive and selective for olefin epoxidation.

Table 1 (Section 2.2) contains  $\Delta H_{\text{CD}_3\text{CN}}$  values for each M- $\beta$  catalyst and Fig. S13 shows that Lewis acid strength (quantified by the value of  $\Delta H_{\text{CD}_3\text{CN}}$ ) appears to correlate linearly with the values of  $E_{\text{Nb}}$ ,  $E_{\text{Ta}}$ ,  $E_{\text{Zr}}$  and  $E_{\text{Hf}}$ , but  $E_{\text{Ti}}$  deviates sharply from this trend. Recently, Román *et al.* measured the chemical shifts of  $^{15}\text{N}$  within labeled pyridine coordinated to defect-less M- $\beta$  materials (using MAS-NMR) and correlated these shifts to the Mulliken electronegativities ( $\chi_x$ , where  $x$  is the metal identity) and calculated (via DFT methods) metal-pyridine bond dissociation energies.<sup>70</sup> Figure S14 shows  $\Delta H_{\text{CD}_3\text{CN}}$  plotted as a function of  $\chi_x$  and suggests that there is no obvious relationship between the measured Lewis acid strength and  $\chi_x$ . The discrepancies in the relationship between Lewis acidity and Pauling/Mulliken electronegativity likely reflects differences in coordination environment of the metal center. For example, group V metals (i.e., Nb and Ta) are penta-coordinated in \*BEA with typically four -O-Si bonds to the framework and an appendage -OH group (i.e., closed sites),<sup>15,71,72</sup> while group IV metals (i.e., Ti, Zr, and Hf) are tetra-coordinated and exist with four framework -O-Si bonds (i.e., closed sites) or three framework bonds and a terminal -OH (i.e., open sites).<sup>19,45,73</sup> Consequently, the reactivity of elements within the same group may correlate with  $E_x$  or  $\chi_x$ ; however, more meaningful comparisons that extend across the periodic-table and which capture potential variations in the coordination of the metal to the zeolite framework require more direct measurements of the properties of the active sites and active intermediates that exist in the catalyst, such as those presented here.

The structure-function relationships elucidated here (Fig. 6) for group IV and V transition metal atoms within a zeolite framework directly oppose the widely-accepted electronic relationships described for homogeneous porphyrin and Schiff-base catalysts.<sup>4,37</sup> These homogeneous complexes are generally constructed to result in increased electron density at the metal center (generally Fe or Mn) to facilitate homolysis of the M-OOH species and yield active oxo (M=O) or oxene (M<sup>+</sup>=O) intermediates. In contrast, epoxidation rates and selectivities of these group IV and V catalysts increase exponentially with Lewis acid strength, while increased electron density (as is beneficial to porphyrin and Schiff-base complexes) on the metal centers would lead to lower epoxidation rates and selectivities.

#### 4.0 CONCLUSIONS

*In situ* UV-vis spectroscopy shows that group IV (i.e., Ti, Zr, and Hf) and V (i.e., Nb and Ta) metal atoms incorporated into the \*BEA zeolite framework activate  $\text{H}_2\text{O}_2$  to form a pool of hydroperoxide, peroxide, and superoxide intermediates. Time resolved UV-vis spectra acquired *in situ* during reaction of  $\text{H}_2\text{O}_2$ -activated materials with  $\text{C}_6\text{H}_{10}$  show that group IV metals react primarily through M-OOH/M-( $\text{O}_2$ )<sup>2-</sup> (i.e., hydroperoxide/peroxide) intermediates, while M-( $\text{O}_2$ )<sup>-</sup> (i.e. superoxide) complexes are the active intermediates on group V metals, which are further confirmed by the isomeric distributions of the epoxide products detected from reaction with Z-stilbene. The dependencies of turnover rates on reactant and product

concentrations, show that these group IV and V catalysts all irreversibly activate  $\text{H}_2\text{O}_2$  to form a pool of M-( $\text{O}_2$ ) intermediates that react with  $\text{C}_6\text{H}_{10}$  or  $\text{H}_2\text{O}_2$  via an Eley-Rideal mechanism to form  $\text{C}_6\text{H}_{10}\text{O}$  or  $\text{H}_2\text{O}_2$ -decomposition products, respectively. Correlation of activation enthalpies for epoxidation and  $\text{H}_2\text{O}_2$  decomposition to  $\text{CD}_3\text{CN}$  adsorption enthalpies reveal that stronger Lewis acids give greater turnover rates and selectivities towards olefin epoxidation. Additionally, activation enthalpies depend strongly on the energy of the LMCT band of the reactive intermediate for each M- $\beta$ , which suggests that metals that more easily pull electron density from the bound-dioxygen intermediates result in a more electrophilic, reactive, and selective intermediates. As such, the design of catalysts with metal centers that are stronger Lewis acids can give both greater reactivity for olefin epoxidation and also greater selectivity and yield for these epoxidations on the basis of  $\text{H}_2\text{O}_2$ . Ongoing investigations in our group seek to understand the relationship between the electronic properties of the reactive intermediates and the steric or electronic properties of various olefins and how the energetics of epoxidation and related oxidation reactions is affected.

#### ASSOCIATED CONTENT

##### Supporting Information.

Characterization data, *in situ* spectroscopic data and processing, and activation enthalpy and entropy determination (PDF) is available free of charge via the Internet at <http://pubs.acs.org>.

##### Notes

The authors declare no competing financial interests.

#### AUTHOR INFORMATION

##### Corresponding Author

\*dwflhrt@illinois.edu

#### ACKNOWLEDGMENTS

We thank Megan Witzke, Neil Wilson, and Pranjali Priyadarshini for insightful discussions, and Dr. Damien Guironnet for helpful discussions and use of lab equipment. DTB was supported by the Department of Defense (DoD) through the National Defense Science & Engineering Graduate Fellowship (NDSEG) Program. This work was carried out in part in the Frederick Seitz Materials Research Laboratory Central Research Facilities at the University of Illinois. This material is based upon work supported, in part by, the U. S. Army Research Office under grant number W911NF-16-1-0128 and the National Science Foundation under grant number CBET-1553137.

#### REFERENCES

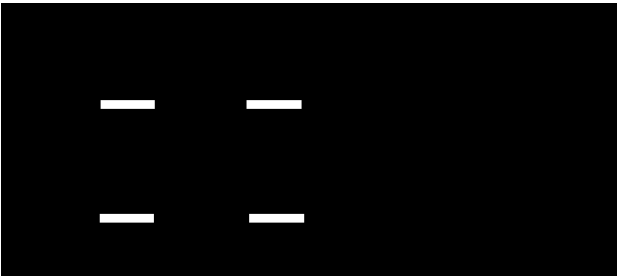
- (1) Czako, B.; Kurti, L. *Strategic Applications of Named Reactions in Organic Synthesis*; Academic Press, 2005.
- (2) Choi, W. J.; Choi, C. Y. *Biotechnology and Bioprocess Engineering* **2005**, *10*, 167-179.
- (3) Lehmhus, D.; Busse, M.; Herrmann, A.; Kayvantash, K. *Structural Materials and Processes in Transportation*; Wiley-VCH: Germany, 2013.
- (4) Wilson, N. M.; Bregante, D. T.; Priyadarshini, P.; Flaherty, D. W. *Catalysis* **2017**, *29*, 122-212.
- (5) Epoxides. In *Ullmann's Encyclopedia of Industrial Chemistry*; Wiley-VCH: Weinheim, Germany, 2012.
- (6) Ethylene Oxide. In *Ullmann's Encyclopedia of Industrial Chemistry*; Wiley-VCH: Weinheim, Germany, 2012.



- (7) *Process Analyzers in Ethylene Oxide Production Plant*, Siemens, 2003.
- (8) Linic, S.; Barteau, M. A. *J. Am. Chem. Soc.* **2003**, *125*, 4034-4035.
- (9) Wen, C.; Yin, A.; Dai, W.-L. *Appl. Catal. B* **2014**, *160-161*, 730-741.
- (10) Obama, B. *Science* **2017**. DOI: 10.1126/science.aam6284
- (11) Campos-Martin, J. M.; Blanco-Brieva, G.; Fierro, J. L. *Angew. Chem. Int. Ed. Engl.* **2006**, *45*, 6962-6984.
- (12) Gleeson, D.; Sankar, G.; Richard A. Catlow, C.; Meurig Thomas, J.; Spanó, G.; Bordiga, S.; Zecchina, A.; Lamberti, C. *Phys. Chem. Chem. Phys.* **2000**, *2*, 4812-4817.
- (13) Carati, A.; Flego, C.; Previde Massara, E.; Millini, R.; Carluccio, L.; Parker, W. O.; Bellussi, G. *Microporous Mesoporous Mater.* **1999**, *30*, 137-144.
- (14) Park, S.; Cho, K. M.; Youn, M. H.; Seo, J. G.; Baeck, S.-H.; Kim, T. J.; Chung, Y.-M.; Oh, S.-H.; Song, I. K. *Catal. Lett.* **2008**, *122*, 349-353.
- (15) Bregante, D. T.; Priyadarshini, P.; Flaherty, D. W. *J. Catal.* **2017**, *348*, 75-89.
- (16) Ruddy, D. A.; Tilley, T. D. *Journal of the American Chemical Society* **2008**, *130*, 11088-11096.
- (17) Thornburg, N. E.; Nauert, S. L.; Thompson, A. B.; Notestein, J. M. *ACS Catal.* **2016**, *6*, 6124-6134.
- (18) Cordeiro, P. J.; Guillo, P.; Spanjers, C. S.; Chang, J. W.; Lipschutz, M. I.; Fasulo, M. E.; Rioux, R. M.; Tilley, T. D. *ACS Catal.* **2013**, *3*, 2269-2279.
- (19) Tang, B.; Dai, W.; Sun, X.; Guan, N.; Li, L.; Hunger, M. *Green Chemistry* **2014**, *16*, 2281-2291.
- (20) Cordeiro, P. J.; Tilley, T. D. *Langmuir* **2011**, *27*, 6295-6304.
- (21) Guo, Y.; Solovyov, A.; Grosso-Giordano, N. A.; Hwang, S.-J.; Katz, A. *ACS Catal.* **2016**, 7760-7768.
- (22) Ouyang, X.; Hwang, S.-J.; Xie, D.; Rea, T.; Zones, S. I.; Katz, A. *ACS Catal.* **2015**, *5*, 3108-3119.
- (23) Thornburg, N. E.; Thompson, A. B.; Notestein, J. M. *ACS Catal.* **2015**, *5*, 5077-5588.
- (24) Srinivas, D.; Manikandan, P.; Laha, S. C.; Kumar, R.; Ratnasamy, P. *J. Catal.* **2003**, *217*, 160-171.
- (25) Lin, W.; Frei, H. *J. Am. Chem. Soc.* **2002**, *124*, 9292-9298.
- (26) Clerici, M. G.; Ingallina, P. *J. Catal.* **1993**, *140*, 71-83.
- (27) Kulkarni, B. S.; Krishnamurthy, S.; Pal, S. *J. Mol. Catal. A: Chem.* **2010**, *329*, 36-43.
- (28) Li, Y.-P.; Head-Gordon, M.; Bell, A. T. *ACS Catal.* **2014**, *4*, 1537-1545.
- (29) Yang, G.; Zhou, L.; Han, X. *J. Mol. Catal. A: Chem.* **2012**, *363-364*, 371-379.
- (30) Luo, H. Y.; Lewis, J. D.; Roman-Leshkov, Y. *Annu Rev Chem Biomol Eng* **2016**, *7*, 663-692.
- (31) Boronat, M.; Corma, A.; Renz, M.; Viruela, P. M. *Chem. Eur. J.* **2006**, *12*, 7067-7077.
- (32) Sastre, G.; Corma, A. *Chem. Phys. Lett.* **1999**, *302*, 447-453.
- (33) Jenzer, G.; Mallat, T.; Maciejewski, M.; Eigenmann, F.; Baiker, A. *Appl. Catal. A* **2001**, *208*, 125-133.
- (34) Bonino, F.; Damin, A.; Bordiga, S.; Carlo, L.; Zecchina, A. *Langmuir* **2003**, *19*, 2155-2161.
- (35) Boronat, M.; Concepción, P.; Corma, A.; Renz, M.; Valencia, S. *J. Catal.* **2005**, *234*, 111-118.
- (36) Boronat, M.; Concepción, P.; Corma, A.; Navarro, M. T.; Renz, M.; Valencia, S. *Phys. Chem. Chem. Phys.* **2009**, *11*, 2876-2884.
- (37) Lane, B. S.; Burgess, K. *Chem. Rev.* **2003**, *103*, 2457-2473.
- (38) Wolf, P.; Hammond, C.; Conrad, S.; Hermans, I. *Dalton Trans.* **2014**, *43*, 4514-4519.
- (39) Dzwigaj, S.; Millot, Y.; Méthivier, C.; Che, M. *Microporous Mesoporous Mater.* **2010**, *130*, 162-166.
- (40) Vega-Vila, J. C.; Harris, J. W.; Gounder, R. *J. Catal.* **2016**, *344*, 108-120.
- (41) Harris, J. W.; Cordon, M. J.; Di Iorio, J. R.; Vega-Vila, J. C.; Ribeiro, F. H.; Gounder, R. *J. Catal.* **2016**, *335*, 141-154.
- (42) Escobedo Morales, A.; Sanchez Mora, E.; Pal, U. *Rev. Mex. Fis. E.* **2007**, *53*, 18-22.
- (43) International Zeolite Association: Verified Syntheses of Zeolitic Materials: Characterization by IR Spectroscopy [http://www.iza-online.org/synthesis/VS\\_2ndEd/IR\\_Spectroscopy.htm](http://www.iza-online.org/synthesis/VS_2ndEd/IR_Spectroscopy.htm) (accessed October 12, 2016)
- (44) Roy, S.; Bakhmutsky, K.; Mahmoud, E.; Lobo, R. F.; Gorte, R. *J. ACS Catal.* **2013**, *3*, 573-580.
- (45) Sushkevich, V. L.; Vimont, A.; Travert, A.; Ivanova, I. I. *J. Phys. Chem. C* **2015**, *119*, 17633-17639.
- (46) Wang, J.; Kispersky, V. F.; Nicholas Delgass, W.; Ribeiro, F. H. *J. Catal.* **2012**, *289*, 171-178.
- (47) Mahmoud, E.; Yu, J.; Gorte, R. J.; Lobo, R. F. *ACS Catal.* **2015**, *5*, 6946-6955.
- (48) Daniell, W.; Topsøe, N. Y.; Knözinger, H. *Langmuir* **2001**, *17*, 6233-6239.
- (49) Tang, B.; Dai, W.; Wu, G.; Guan, N.; Li, L.; Hunger, M. *ACS Catal.* **2014**, *4*, 2801-2810.
- (50) Sushkevich, V. L.; Palagin, D.; Ivanova, I. I. *ACS Catal.* **2015**, *5*, 4833-4836.
- (51) Madon, R. J.; Boudart, M. *Ind. Eng. Chem. Fundam.* **1982**, *21*, 438-447.
- (52) Shetti, V. N.; Manikandan, P.; Srinivas, D.; Ratnasamy, P. *J. Catal.* **2003**, *216*, 461-467.
- (53) Brutchey, R. L.; Ruddy, D. A.; Andersen, L. K.; Tilley, T. D. *Langmuir* **2005**, *21*, 9576-9583.
- (54) Morlanés, N.; Notestein, J. M. *Appl. Catal. A* **2010**, *387*, 45-54.
- (55) Chen, C.; Yuan, H.; Wang, H.; Yao, Y.; Ma, W.; Chen, J.; Hou, Z. *ACS Catal.* **2016**, *6*, 3354-3364.
- (56) Yoon, C. W.; Hirsekorn, K. F.; Neidig, M. L.; Yang, X.; Tilley, T. D. *ACS Catal.* **2011**, *1*, 1665-1678.
- (57) Bravo-Suárez, J. J.; Bando, K. K.; Lu, J.; Haruta, M.; Fujitani, T.; Oyama, S. T. *J. Phys. Chem. C* **2008**, *112*, 1115-1123.
- (58) Ziolek, M.; Sobczak, I.; Decyk, P.; Sobańska, K.; Pietrzyk, P.; Sojka, Z. *Appl. Catal. B* **2015**, *164*, 288-296.
- (59) Ziolek, M.; Sobczak, I.; Decyk, P.; Wolski, L. *Catal. Commun.* **2013**, *37*, 85-91.
- (60) Bonino, F.; Damin, A.; Ricchiardi, G.; Ricci, M.; Spano, G.; D'Aloisio, R.; Zecchina, A.; Lamberti, C.; Prestipino, C.; Bordiga, S. *J. Phys. Chem. B* **2008**, *108*, 3573-3583.
- (61) Wang, L.; Xiong, G.; Su, J.; Li, P.; Guo, H. *J. Phys. Chem. C* **2012**, *116*, 9122-9131.
- (62) Notari, B. *Adv. Catal.* **1996**, *41*, 253-334.
- (63) Sams, C. K.; Jørgensen, K. A. *Acta Chem. Scand.* **1995**, *49*, 839-847.
- (64) Raj, N. K. K.; Ramaswamy, A. V.; Manikandan, P. *J. Mol. Catal. A: Chem.* **2005**, *227*, 37-45.
- (65) Bordiga, S.; Damin, A.; Bonino, F.; Ricchiardi, G.; Lamberti, C.; Zecchina, A. *Angew. Chem. Int. Ed. Engl.* **2002**, *41*, 4734-4737.
- (66) Pauling, L. *J. Am. Chem. Soc.* **1932**, *54*, 3571-3582.
- (67) Rohrer, G. S. *Structure and Bonding in Crystalline Materials*; Cambridge University Press, 2001.
- (68) Anslyn, E. V.; Dougherty, D. A. *Modern Physical Organic Chemistry*; University Science, 2005.
- (69) Clerici, M. G. *Kinet. Catal.* **2015**, *56*, 450-455.
- (70) Gunther, W. R.; Michaelis, V. K.; Griffin, R. G.; Román-Leshkov, Y. *J. Phys. Chem. C* **2016**, *120*, 28533-28544.
- (71) Tielens, F.; Shishido, T.; Dzwigaj, S. *J. Phys. Chem. C* **2010**, *114*, 3140-3147.
- (72) Dzwigaj, S.; Millot, Y.; Che, M. *Catal. Lett.* **2010**, *135*, 169-174.
- (73) Wang, Y.; Lewis, J. D.; Román-Leshkov, Y. *ACS Catal.* **2016**, 2739-2744.

SYNOPSIS TOC

1  
2  
3  
4  
5  
6  
7  
8  
9  
10  
11  
12  
13  
14  
15  
16  
17  
18  
19  
20  
21  
22  
23  
24  
25  
26  
27  
28  
29  
30  
31  
32  
33  
34  
35  
36  
37  
38  
39  
40  
41  
42  
43  
44  
45  
46  
47  
48  
49  
50  
51  
52  
53  
54  
55  
56  
57  
58  
59  
60



---